Cell Reports Methods, Volume *4*

Supplemental information

Discovery and generalization of tissue structures from spatial omics data

Zhenqin Wu, Ayano Kondo, Monee McGrady, Ethan A.G. Baker, Benjamin Chidester, Eric Wu, Maha K. Rahim, Nathan A. Bracey, Vivek Charu, Raymond J. Cho, Jeffrey B. Cheng, Maryam Afkarian, James Zou, Aaron T. Mayer, and Alexandro E. Trevino

Table of Contents:

Supplementary Figures

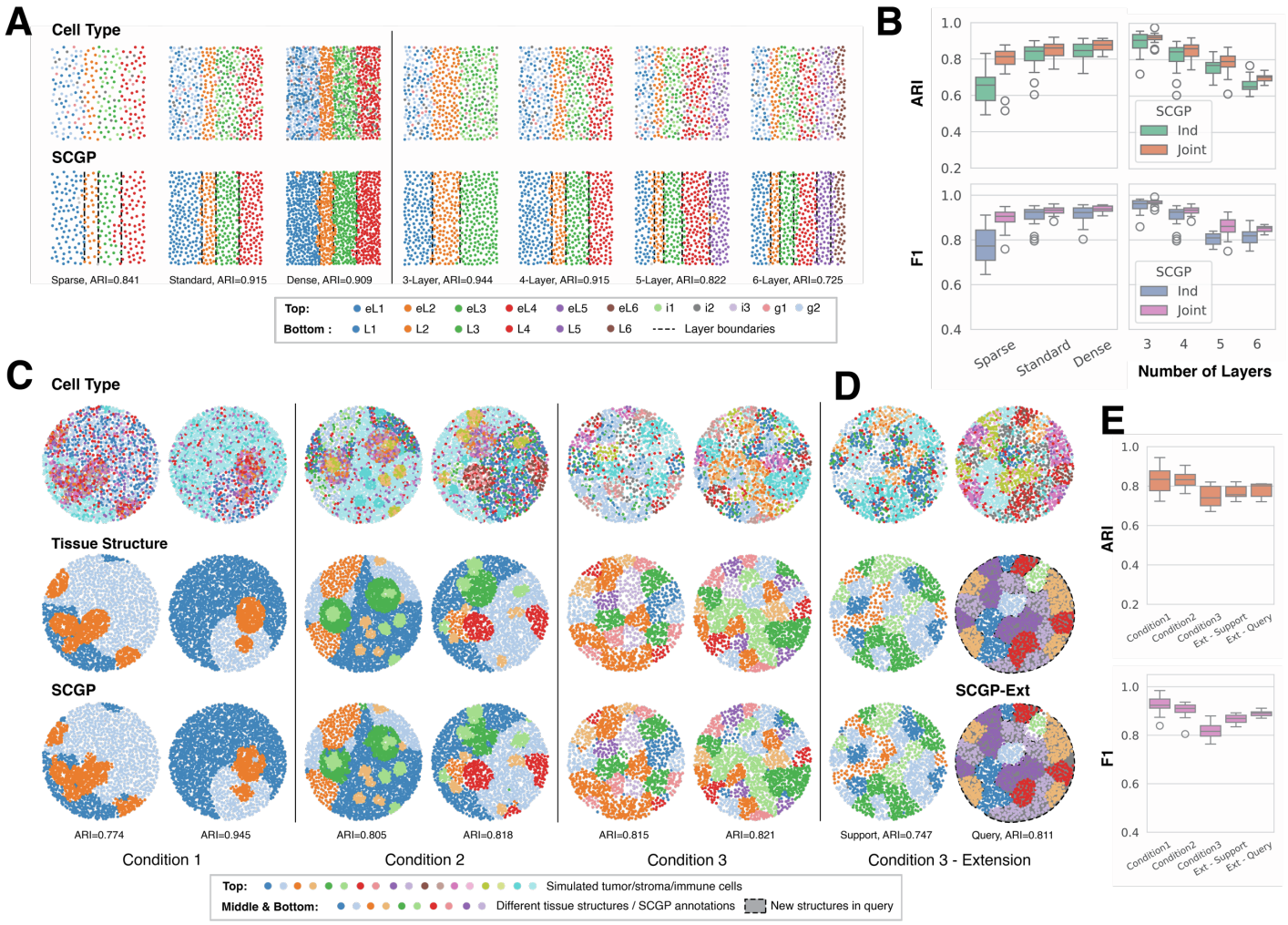

Figure S1. SCGP partitioning of simulation data, related to Figure 1.

A. Simulated data is adopted from Chidester et al.[s1], which modeled the structure of the mouse cortex. Each simulated layer of the cortex consists of different combinations of glial cells, excitatory and inhibitory neurons (e.g., eL1, i1, g1). SCGP identified ground truth layer structures across diverse settings (i.e., cell density, number of layers). **B.** Quantitative measurements revealed that joint clustering of multiple samples derived from the same data distribution always yield better performances than independent clustering**.** Notably, thinner layers (2-3 cells) are typically more challenging to recognize. **C.** SCGP identified ground truth tissue structures in TMA data simulated using different strategies: Condition 1 consists of a base layer and two major structures; Condition 2 consists of a base layer and a much wider variety of tissue structures; Condition 3 defines segments of equal sizes and assigns them to different tissue structures randomly. Cells are sampled for each tissue structure based on a predefined cell type composition mapping. Note that both cell types and biomarker expression are directly sampled from a real head-and-neck cancer dataset[s2] that we have previously studied. **D.** In condition 3 simulation, we explicitly add novel structures (e.g., red, purple partitions) to the query samples. SCGP-Extension successfully recognized both known and novel tissue structures across all query samples, achieving comparable or superior accuracy to the reference samples. **E.** SCGP and SCGP-Extension achieved robust performances (ARI > 0.7) across diverse simulated TMA data regardless of shapes and complexities (i.e., 10+ tissue structures).

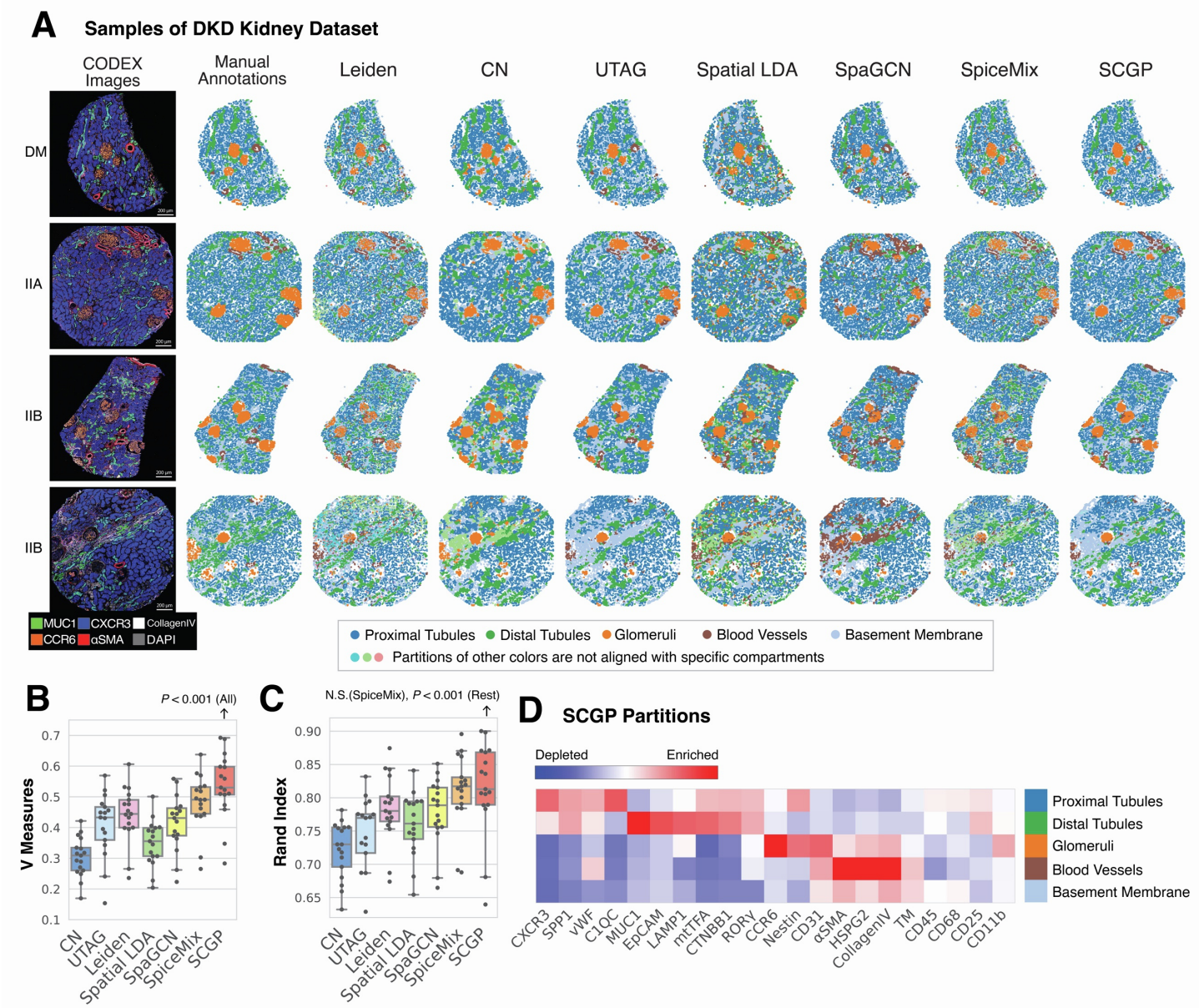

Figure S2. More examples from the DKD Kidney dataset, related to Figure 2.

A. Clustering/partitioning outputs from unsupervised annotation tools on four samples of different DKD classes are illustrated. Qualitatively, Leiden clustering identified cell types that are not spatially smooth; CN defined an extra cluster (cyan) for proximal tubules; UTAG defined multiple smaller clusters (light green, gray, purple) that do not correspond to any compartments; Spatial LDA and SpiceMix had more noisy annotations for glomeruli (orange); SpaGCN misrecognized some regions as blood vessels; SCGP misrecognized some fibrotic glomeruli as blood vessels. **B-C.** Additional quantitative metrics (V measures and Rand index) show consistent results. *P* values are calculated using the Wilcoxon signed-rank test. **D.** Full heatmap for all biomarkers tested in the DKD Kidney dataset shows signature protein biomarkers for SCGP partitions, with each partition corresponding to a manually annotated compartment.

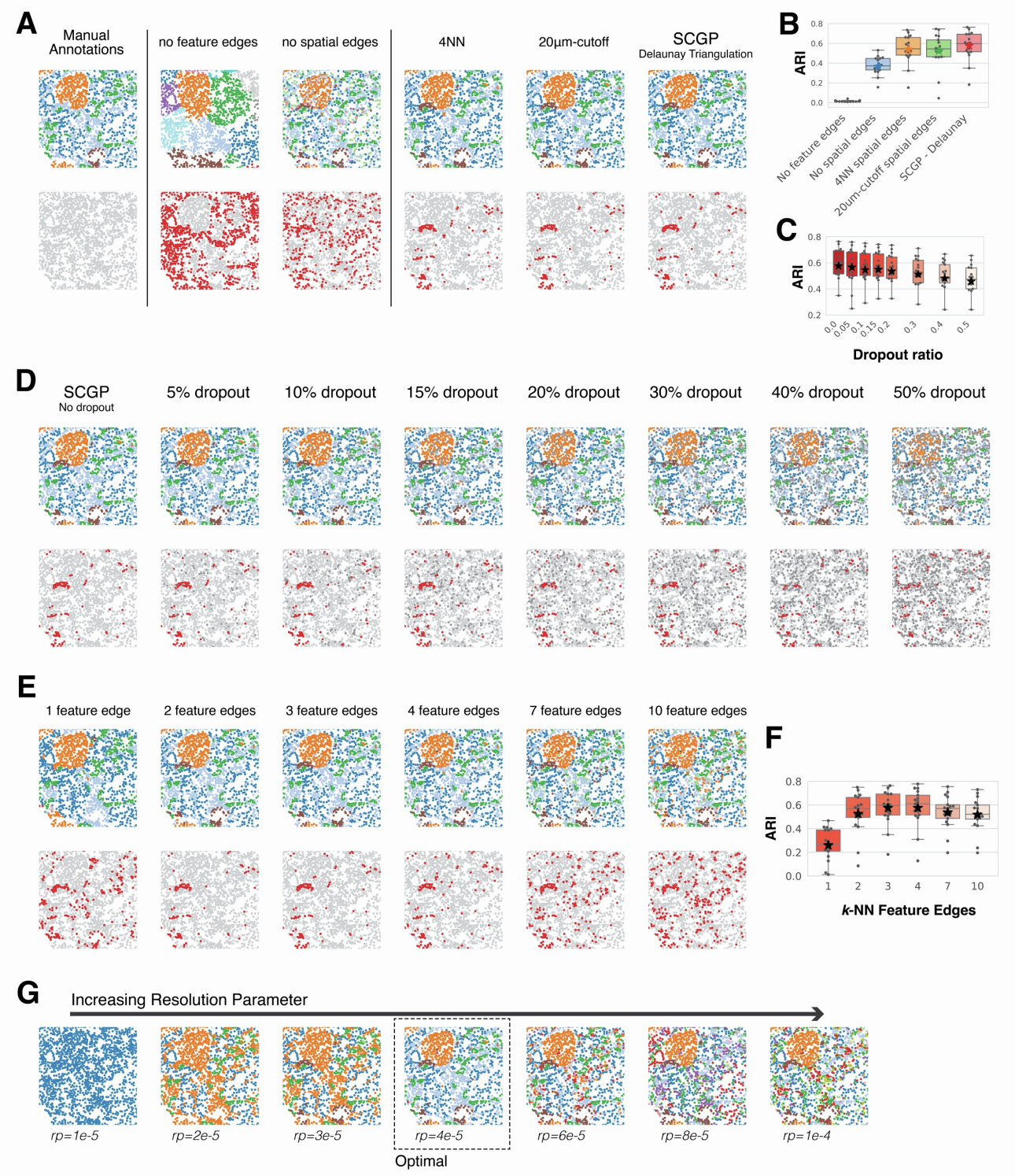

Figure S3. Ablation experiments on the DKD Kidney dataset, related to Figure 2.

A. SCGP established a hybrid graph consisting of spatial edges and feature edges. Excluding either component will cause major performance decay: Excluding spatial edges degrades SCGP to a vanilla Leiden clustering, resulting in noisy and unsmooth partitions; Excluding feature edges disconnects distant tissue structures and leads to inconsistent outputs. Switching the type of spatial edges does not significantly change outputs. **B.** ARIs of different variants show consistent results as observed in panel A. **C-D.** To evaluate how segmentation noise might affect partition outcome, we experimented with randomly excluding nodes/cells from the graph. Outcomes and performances are robust and stable even after 20% dropout. **E-F.** We examined the influence of a hyperparameter choice: num of feature edges. More feature edges (>5) resulted in fragmented partitions and worse alignment. Optimal performances were observed when the number of edges is set between 2 and 4 in this experiment. **G.** Granularity of the partition outcomes can be controlled by the resolution parameter.

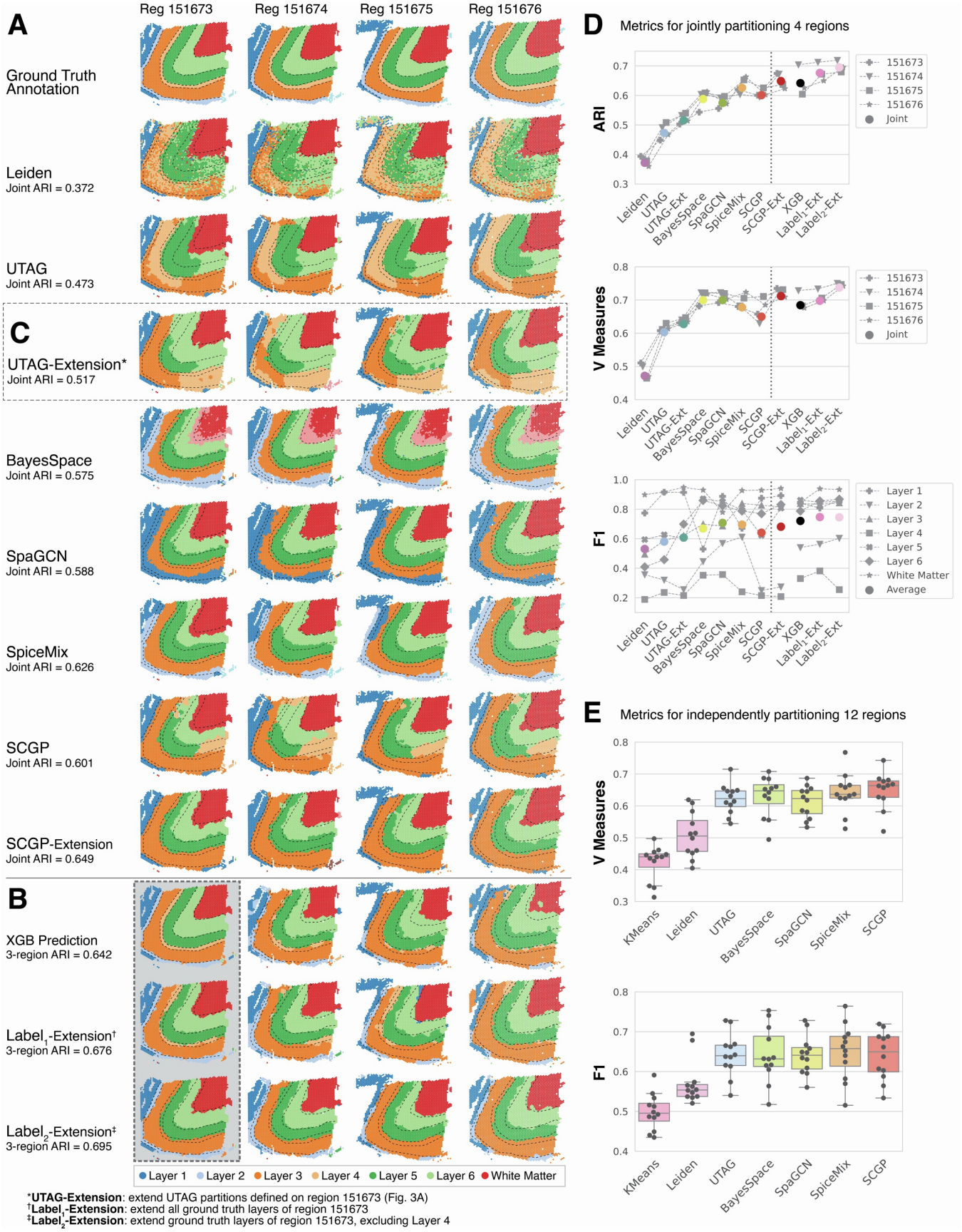

Figure S4. Partitioning of DLPFC samples, related to Figure 3.

A. Joint unsupervised annotations recognized major layers in four DLPFC samples. Notably, characterization of the two thinner layers (Layer 2 and Layer 4) were worse in most methods. **B.** Approaches utilizing partial ground truth annotations were examined.(continued)

(continued) The predictive modeling approach trained a gradient boosted tree model (XGBoost) with the ground truth annotations and applied it to the rest. SCGP-Extension can be adapted with ground truth annotations as references. The $Label_2$-Extension variant demonstrated the best performances. **C.** SCGP-Extension can be applied with noisy references: when using UTAG annotations (fitted on Reg 151673) as references, resulting query partitions did not show better alignment with ground truth, but captured the same spatial compartmentalization patterns as the reference region. **D.** Quantitative metrics show performances of unsupervised annotation tools. Methods utilizing partial ground truth achieved best performances, in which extensions of ground truth labels performed better than XGBoost predictions. **E.** Additional quantitative metrics (V measures and F1 scores) were calculated for independent partitioning of all samples in DLPFC and show consistent results.

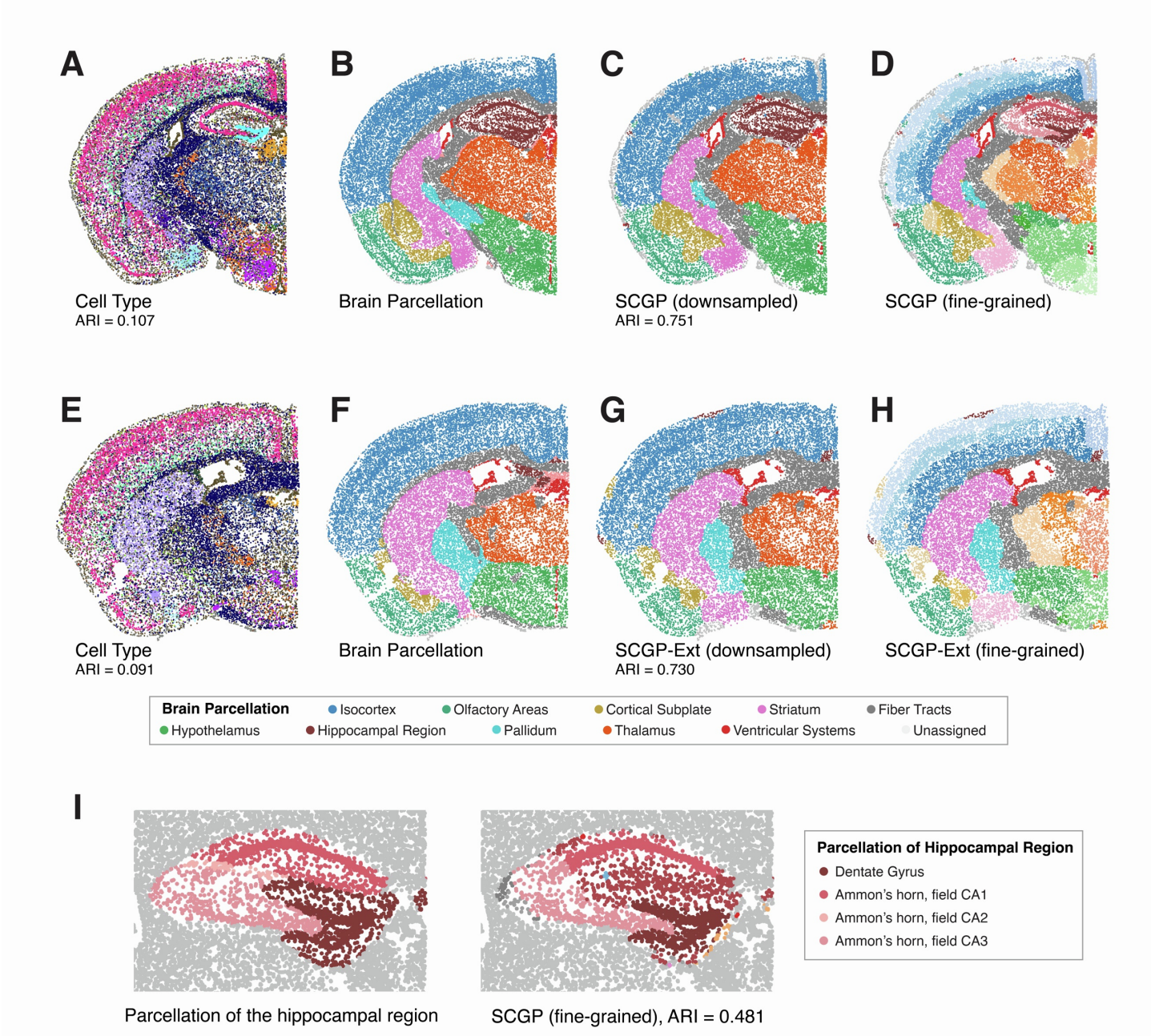

Figure S5. SCGP annotations of mouse brain sections, related to Figure 3.
A. Cell types were annotated for a coronal mouse brain section. Please refer to Zhang et al.[s3] for color details. **B.** Cells were further mapped to Allen CCFv3 to annotate brain parcels. **C.** SCGP accurately identified major parcels, achieving an ARI score of 0.751. **D.** Fine-grained SCGP identified more fine-grained structures. Note the layered structures in isocortex, which can be robustly extended to the query section (panel H). **E-H.** Cells in another distant section were annotated and partitioned using the reference section (panel C-D) and SCGP-Extension, which yielded consistent results, both visually and quantitatively, with an ARI score of 0.730. **I.** SCGP with higher granularity identified fine-grained structures in the hippocampal region.

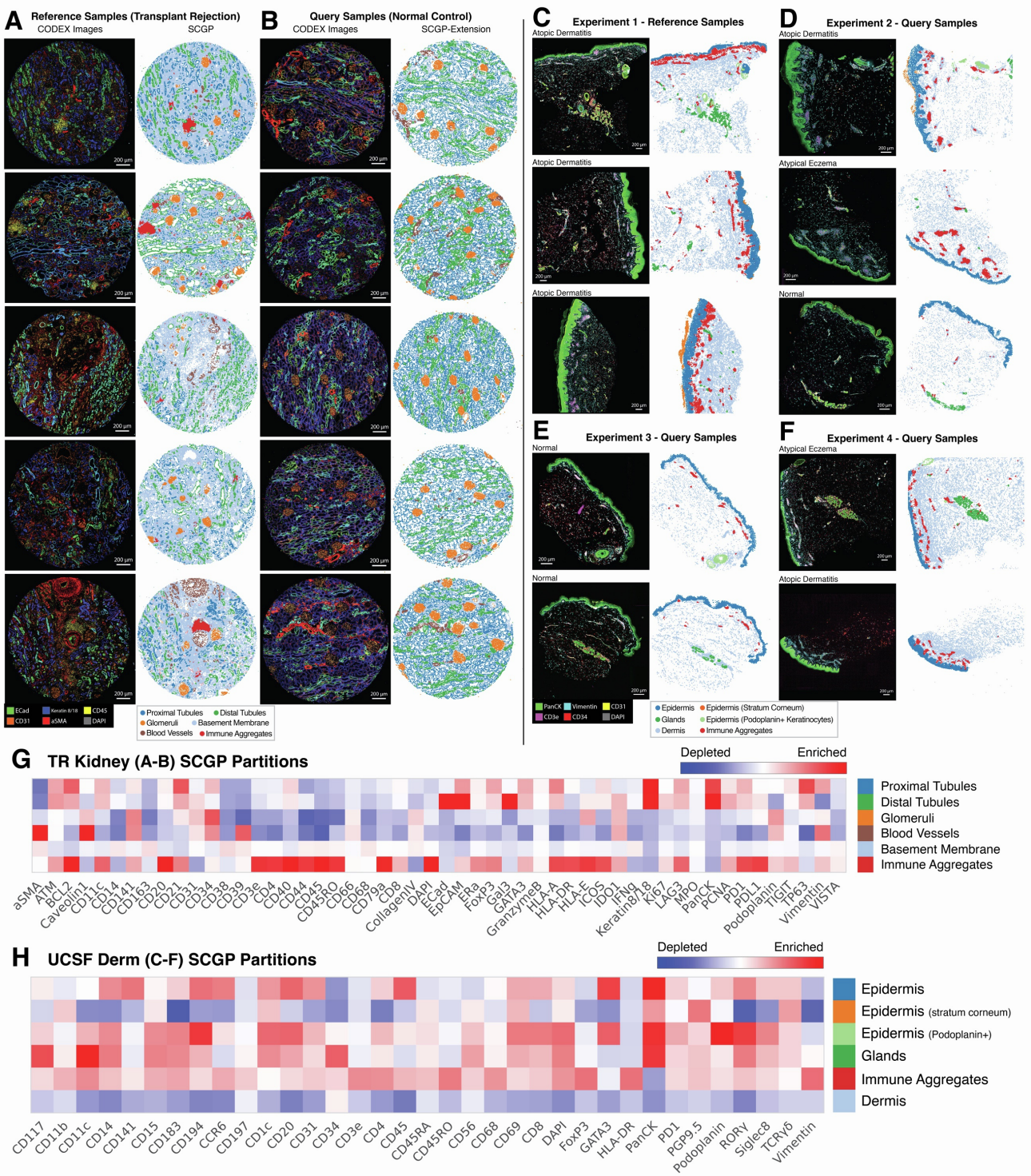

Figure S6. SCGP annotations of TR Kidney dataset and UCSF Derm dataset, related to Figure 4.

A. Primary SCGP experiment on 10 samples from the TR Kidney dataset with heavy inflammation defined six major partitions corresponding to kidney tissue structures including tubules, glomeruli, and blood vessels. The red partition exhibits high expression of immune cell biomarkers, suggesting substantial immune cell infiltration. **B.** Partitions were extended to 5 normal samples from the TR Kidney dataset that have minimal inflammation. Note the absence of the immune aggregates partition and the denser arrangement of tubules and glomeruli. **C.** Primary SCGP annotations on 17 samples from experiment 1 of the UCSF Derm dataset defined major tissue structures including the epidermis layers, dermis layer, immune aggregates, and glands. **D-F.** Partitions were extended to samples from different experiments of the UCSF Derm dataset, yielding consistent annotations. **G.** Signature protein biomarker expression of the six kidney tissue structures are visualized in the heatmap. Note that the same set of kidney tissue structures as in Fig. 2D were derived despite the fact that TR Kidney dataset used a different biomarker panel. **H.** Signature protein biomarker expression for the major skin partitions identified by SCGP are visualized in the heatmap.

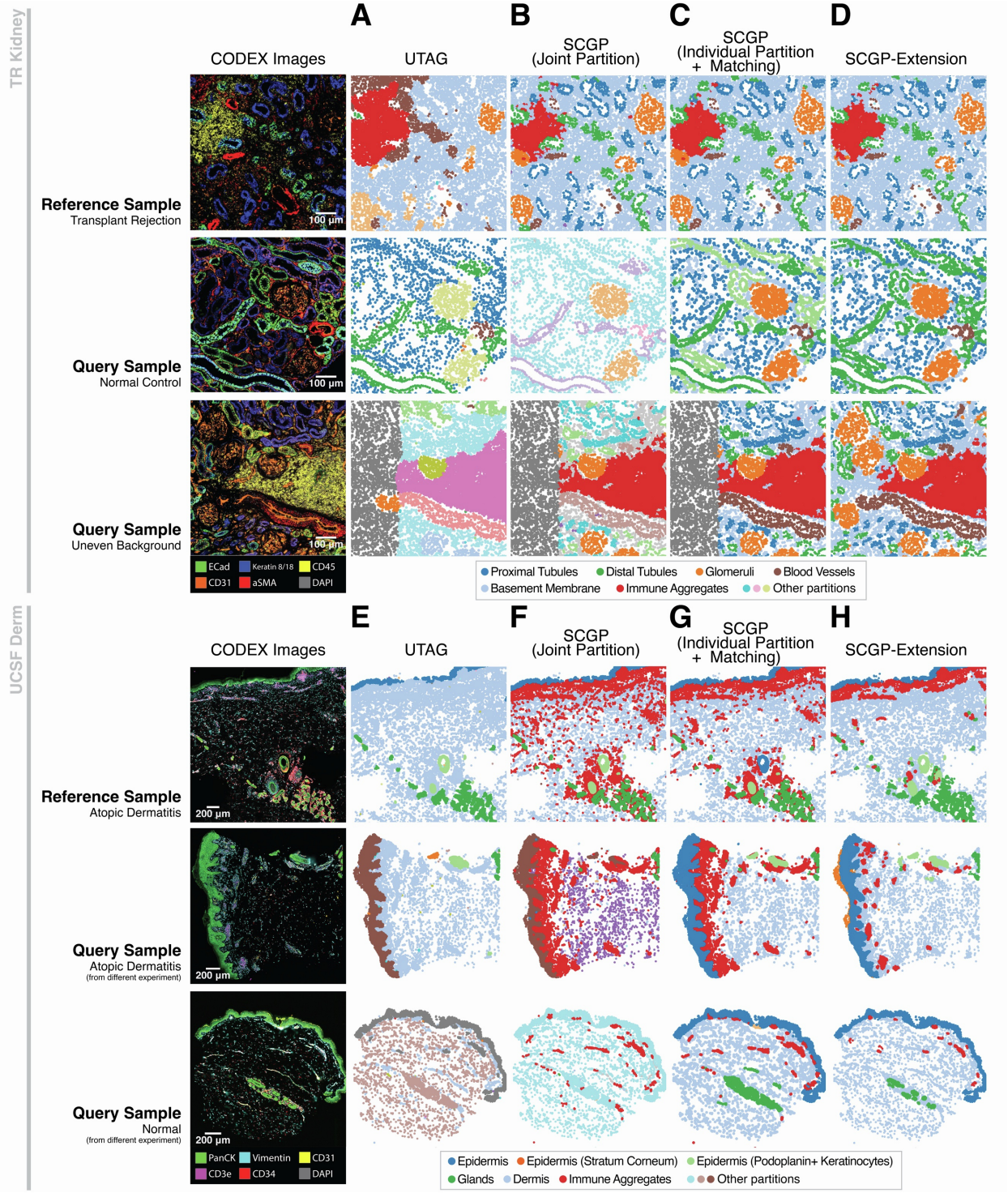

Figure S7. Annotating representative samples from TR Kidney dataset and UCSF Derm dataset using variants of SCGP, related to Figure 4.

On a set of representative samples from the TR kidney dataset, A. UTAG defined partitions do not correspond well to tissue structures. **B.** SCGP failed to assign tissue structures from different conditions into the same partition. Note the different colors. **C.** Individual SCGP partitions of different samples were matched post hoc to reflect shared tissue structures. Note the vertical separation of partitions due to uneven background. **D.** SCGP-Extension enabled consistent recognition of tissue structures regardless of artifact and different disease conditions. **On a set of representative samples from the UCSF derm dataset, E-F.** Joint partitioning with UTAG and SCGP failed to assign tissue structures from different experiments into the same partition. Note the different colors of epidermal layers in the samples. **G.** Individual partitions of different samples were matched post hoc to reflect shared tissue structures. **H.** Reference-query extension pipeline enabled consistent recognition of tissue structures across samples from multiple experiments with different skin conditions.

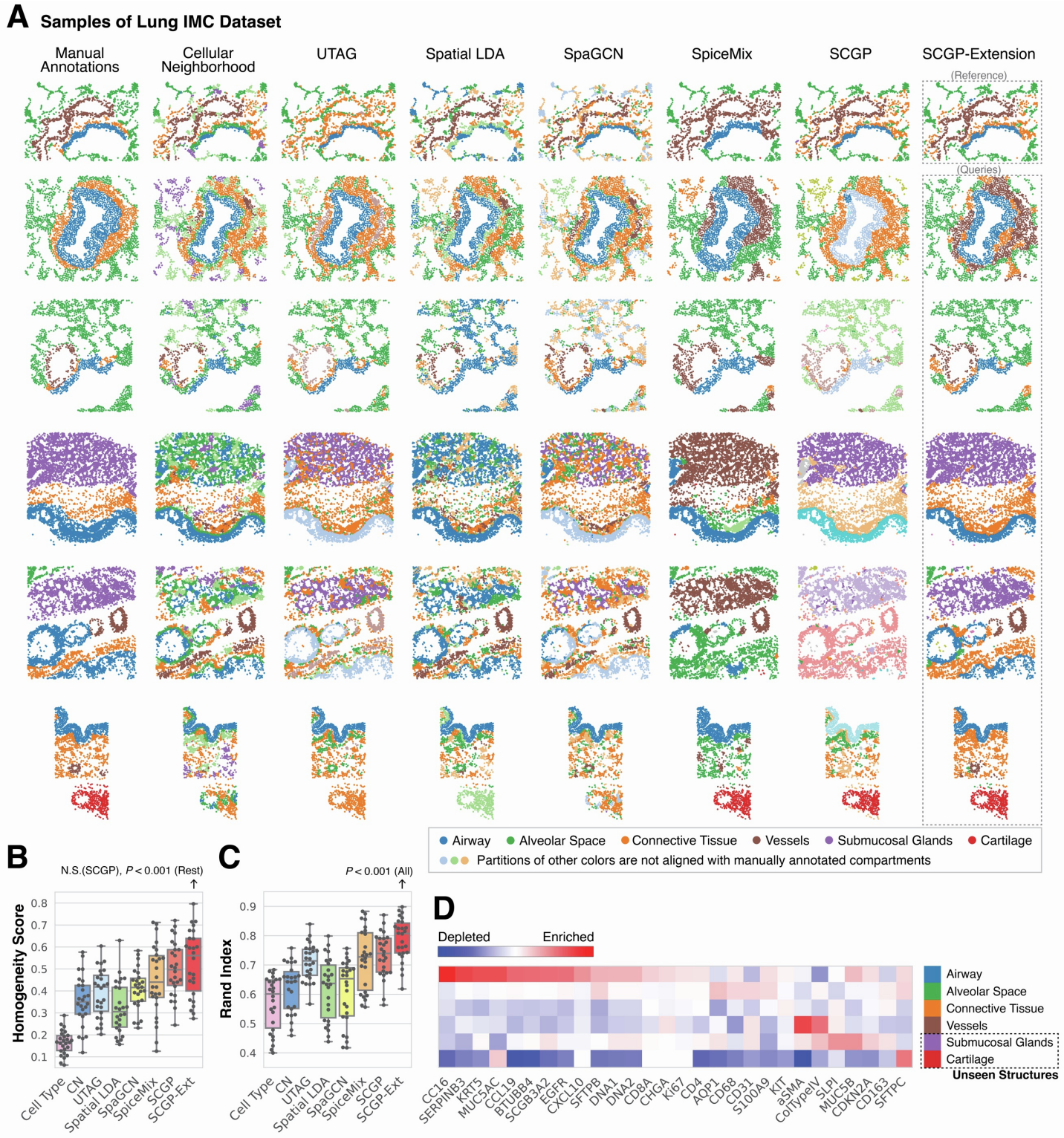

Figure S8. SCGP annotations of Lung IMC dataset, related to Figure 4.

A. Clustering/partitioning outputs from various unsupervised annotation tools on representative lung samples are visualized. When jointly partitioning all 26 samples, one class of tissue structures from different samples is usually assigned to disconnected partitions, as evidenced by the diverse colors. SCGP-Extension resolved the issue by extending reference partitions defined on a well-integrated subset of seven samples. Resulting partitions on the remaining samples demonstrated the best visual alignment with manual annotations. **B-C.** Quantitative metrics[s4] (homogeneity score and rand index) show that SCGP-Extension achieved the best performance. *P* values are calculated using the Wilcoxon signed-rank test. **D.** Signature protein biomarker expression for the tissue structures identified by SCGP-Extension are visualized in the heatmap, corresponding to the six manually annotated compartments. Note that submucosal glands and cartilage are two novel tissue structures revealed in the query samples by SCGP-Extension

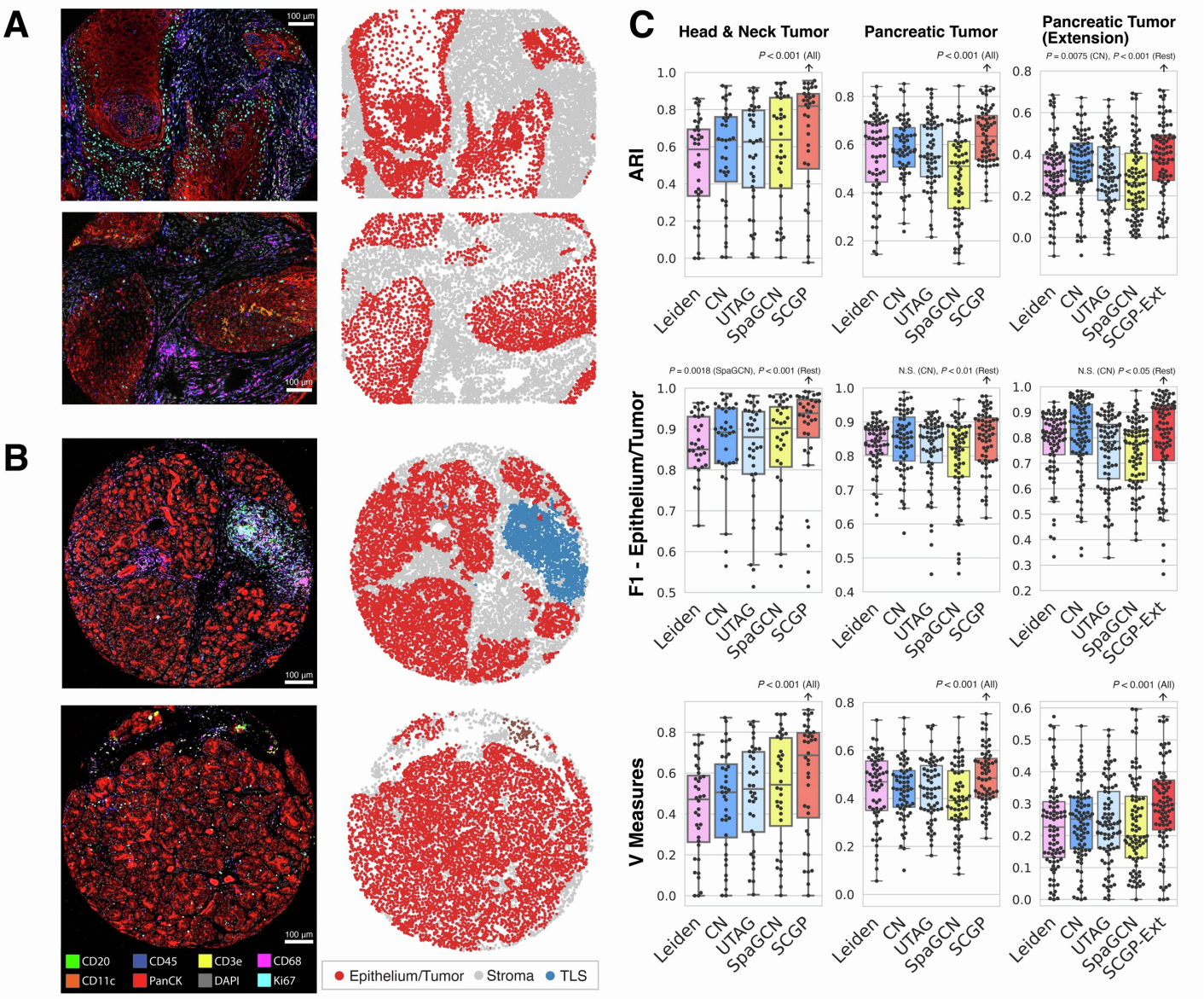

Figure S9. Identification of tumor/stroma regions in tumor microenvironments, related to Figure 6.

A. Tumor and stroma regions in the representative samples from UPMC-HNC were annotated by SCGP. **B.** Structures in the representative samples from the Stanford-PC dataset were annotated by SCGP. 148 tumor cores from this dataset were divided into two subsets: 63 and 85 cores respectively as reference and query sets for validating SCGP-Extension. Note the blue partition that indicates a tertiary lymphoid structure. **C.** Quantitative metrics (ARI, F1 scores, V measures) were calculated for all unsupervised annotation methods, in which SCGP/SCGP-Extension achieved superior performances. *P* values are calculated using the Wilcoxon signed-rank test.

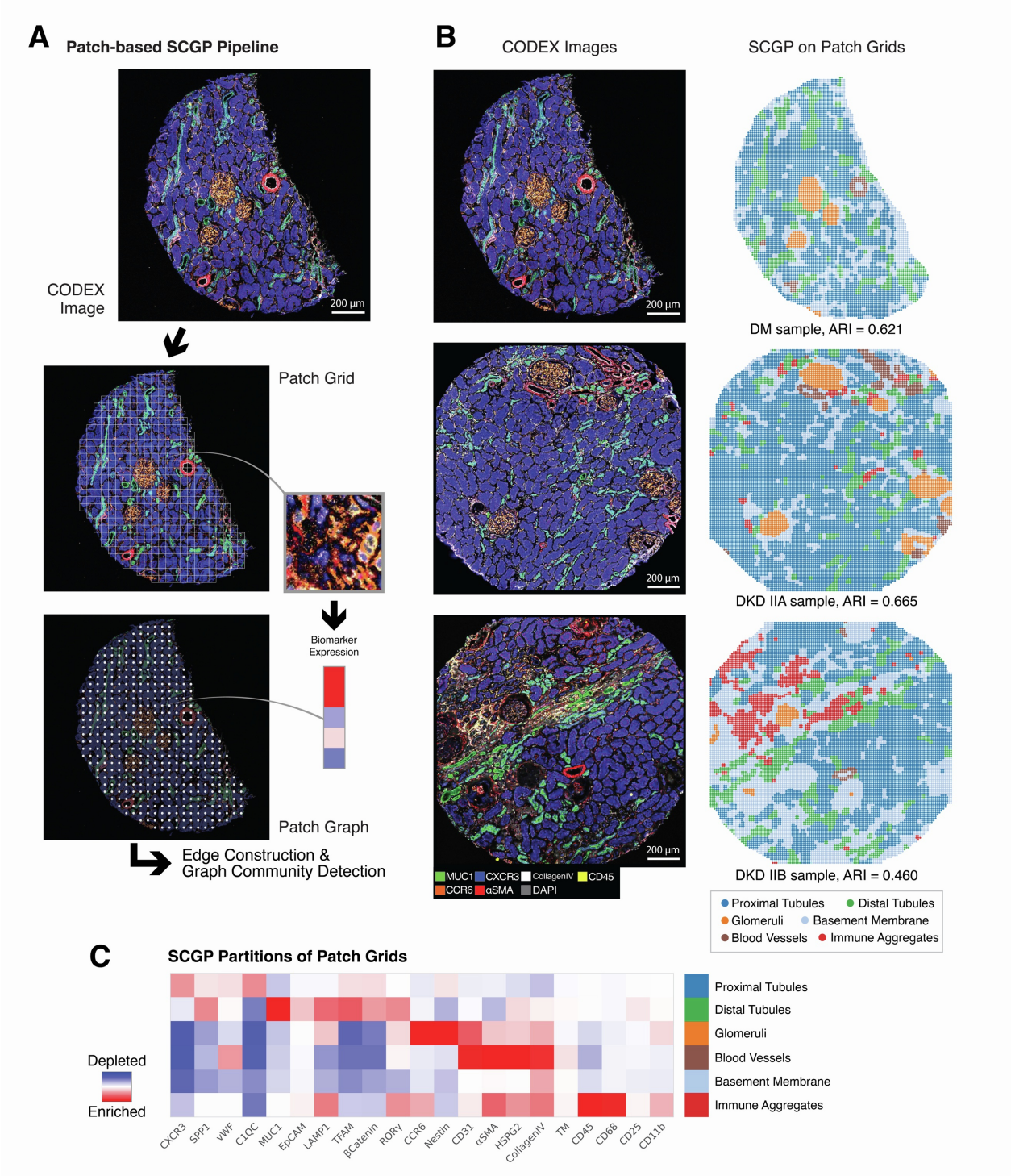

Figure S10. SCGP annotations of mIF images as spatial grids of patches, related to STAR Methods.

A. In the absence of cell segmentation, mIF images can be directly partitioned using SCGP by adopting a spatial-grid approach: Images were first dissected into small patches through a sliding window. Nodes were defined based on patches, with node features summarizing biomarker expression in the patches. Spatial edges and feature edges were constructed in a similar fashion to enable application of SCGP. Note that the resolution of the grid can be adjusted by varying the size of the patches. **B.** SCGP on the patch grids of three mIF images yielded similar results as cell-based SCGP, recognizing tubules, glomeruli, blood vessels, and immune aggregates in the tissue. In the severe DKD (IIB) sample, the fibrotic glomeruli were recognized as combinations of the basement membrane and normal glomeruli partitions, suggesting the degradation of normal glomerular structures into scar tissues. **C.** Signature protein biomarker expressions are visualized in the heatmap for the partitions identified by patch-based SCGP. Note the distinct immune aggregates partition enriched in CD45, CD68, and DAPI (i.e., higher cell density).

Supplementary Tables

Table S1. Details of datasets: number of samples/cells/patients, major grouping or patient characteristics, related to STAR Methods.

Dataset	N (samples)	N (cells/spots)	N (patients)	Major groups / patient characteristics
DKD Kidney	17	137,654	12	Kidney sections with different DKD classes: ● Healthy kidneys from diabetic individuals (DM): 7 sections ● DKD class IIA: 2 sections ● DKD class IIA-B: 3 sections ● DKD class IIB: 4 sections ● DKD class III: 1 section
DLPFC	12	47,681	3	Postmortem DLPFC samples from three independent neurotypical adult donors.
ABCA-1	2	57,731	1	MERFISH spatial transcriptomics dataset of a single adult mouse brain. Parcellation is defined by aligning cells to the 3D Allen-CCF.
TR Kidney	22	765,129	22	Kidney samples sorted into two groups: ● Case group: 17 samples (transplant rejection) ● Control group: 5 samples (normal)
Lung IMC	26	69,830	3	Lung samples from three healthy donor lung specimens: sections of airways extending from proximal bronchi and succeeding divisions to terminal and respiratory bronchioles.
UCSF Derm	44	588,867	33	Skin samples with different skin conditions: ● Atopic Dermatitis (AD) ● Normal (N) The dataset is collected from 4 experiments: ● Experiment 1: 22 samples (22 AD) ● Experiment 2: 11 samples (4 AD, 4 N) ● Experiment 3: 3 samples (3 N) ● Experiment 4: 8 samples (2 AD, 3 N)
UPMC-HNC	36	175,698	24	Tumor cores from a cohort of head-and-neck cancer patients.
Stanford-PC	148	815,463	148	Tumor cores from a cohort of pancreatic cancer patients, separated into two subsets containing 63 and 85 cores each.

Table S2. Running time and memory usage of unsupervised annotation methods, related to STAR Methods.

Method	DKD Kidney (17 samples, 137,654 cells)		DLPFC (4 samples, 14,364 spots)
	Time	Memory (Peak)	Time
KMeans	<10s KMeans: 2s	179 MB	<10s KMeans: 1s
Leiden[s5]	1min Leiden: 50s	2792 MB	<10s Leiden: 5s
CN[s6]	24s Composition vectors: 22s KMeans: 2s	61 MB	N/A
UTAG[s4]	2min Aggregate expression: 53s Leiden: 50s	2426 MB	12s Aggregate expression: 7s Leiden: 5s
Spatial LDA[s7]	25min Count vectors + spatial prior: 30s LDA: 1500s	64.6 GB	N/A
BayesSpace[s8]	N/A	N/A	17min Parameter estimation: 1030s
SpaGCN[s9]	7min Construct graph: 68s GCN optimization: 360s	282.7 GB	23s Construct graph: 3s GCN optimization: 20s
SpiceMix[s1]	4.5h Construct graph: 10s Louvain: 1000s Optimization (100 iterations): 15000s	11.48 GB	1.25h Construct graph: 5s Louvain: 30s Optimization (200 iterations): 4500s
SCGP	1min Construct graph: 30s Leiden: 30s	1434 MB	<10s Construct graph: 2s Leiden: 2s
SCGP-Extension	2min Reference SCGP (14 samples): 55s Pseudo-nodes: 10s Query extension (3 samples): 60s	1125 MB	10s Reference SCGP (1 sample): 1s Pseudo-nodes: 1s Query extension (3 samples): 8s

References

s1. Chidester, B., Zhou, T., Alam, S., and Ma, J. (2023). SPICEMIX enables integrative single-cell spatial modeling of cell identity. Nat. Genet. *55*, 78–88. 10.1038/s41588-022-01256-z.

s2. Wu, Z., Trevino, A.E., Wu, E., Swanson, K., Kim, H.J., D'Angio, H.B., Preska, R., Charville, G.W., Dalerba, P.D., Egloff, A.M., et al. (2022). Graph deep learning for the characterization of tumour microenvironments from spatial protein profiles in tissue specimens. Nat Biomed Eng *6*, 1435–1448. 10.1038/s41551-022-00951-w.

s3. Zhang, M., Pan, X., Jung, W., Halpern, A.R., Eichhorn, S.W., Lei, Z., Cohen, L., Smith, K.A., Tasic, B., Yao, Z., et al. (2023). Molecularly defined and spatially resolved cell atlas of the whole mouse brain. Nature *624*, 343–354. 10.1038/s41586-023-06808-9.

s4. Kim, J., Rustam, S., Mosquera, J.M., Randell, S.H., Shaykhiev, R., Rendeiro, A.F., and Elemento, O. (2022). Unsupervised discovery of tissue architecture in multiplexed imaging. Nat. Methods *19*, 1653–1661. 10.1038/s41592-022-01657-2.

s5. Traag, V.A., Waltman, L., and van Eck, N.J. (2019). From Louvain to Leiden: guaranteeing well-connected communities. Sci. Rep. *9*, 1–12. 10.1038/s41598-019-41695-z.

s6. Schürch, C.M., Bhate, S.S., Barlow, G.L., Phillips, D.J., Noti, L., Zlobec, I., Chu, P., Black, S., Demeter, J., McIlwain, D.R., et al. (2020). Coordinated Cellular Neighborhoods Orchestrate Antitumoral Immunity at the Colorectal Cancer Invasive Front. Cell *183*, 838. 10.1016/j.cell.2020.10.021.

s7. Chen, Z., Soifer, I., Hilton, H., Keren, L., and Jojic, V. (2020). Modeling Multiplexed Images with Reveals Novel Tissue Microenvironments. J. Comput. Biol. *27*, 1204–1218. 10.1089/cmb.2019.0340.

s8. Zhao, E., Stone, M.R., Ren, X., Guenthoer, J., Smythe, K.S., Pulliam, T., Williams, S.R., Uytingco, C.R., Taylor, S.E.B., Nghiem, P., et al. (2021). Spatial transcriptomics at subspot resolution with BayesSpace. Nat. Biotechnol. *39*, 1375–1384. 10.1038/s41587-021-00935-2.

s9. Hu, J., Li, X., Coleman, K., Schroeder, A., Ma, N., Irwin, D.J., Lee, E.B., Shinohara, R.T., and Li, M. (2021). SpaGCN: Integrating gene expression, spatial location and histology to identify spatial domains and spatially variable genes by graph convolutional network. Nat. Methods *18*, 1342–1351. 10.1038/s41592-021-01255-8.